Journal of
Materials Chemistry B

Materials for biology and medicine

Accepted Manuscript

This article can be cited before page numbers have been issued, to do this please use: W. Yang, X. Wang, W. Hao, Q. Wu, J. Peng, J. Tu and Y. Cao, *J. Mater. Chem. B*, 2020, DOI: 10.1039/D0TB00082E.




ROYAL SOCIETY OF CHEMISTRY

rsc.li/materials-b

View Article Online
DOI: 10.1039/D0TB00082E

ARTICLE

# 3D hollow-out $TiO_2$ nanowire cluster / GOx as ultrasensitive photoelectrochemical glucose biosensor

Received 00th January 20xx,
Accepted 00th January 20xx

DOI: 10.1039/x0xx00000x

Wenke Yang,[a] Xiaohong Wang,[a] Wanjun Hao,[*a] Qiang Wu,[*b] Juan Peng,[c] Jinchun Tu,[a] and Yang Cao,[a,d]

Ultra-high sensitivity is difficult to achieve using conventional enzymatic glucose biosensors due to the lack of exposed active sites and steric-hinderance effect. Thus, in the present work, we report a photoelectrochemical (PEC) enzymatic glucose biosensor based on 3-dimensional (3D) hollow-out titanium dioxide ($TiO_2$) nanowire clusters (NWc)/ glucose oxidase (GOx), with providing more exposed active sites, constructing a sensor with a higher affinity toward glucose reaction. Excellent performance with an ultra-high sensitivity of 58.9 μA $mM^{-1}$ $cm^{-2}$, 0-2 mM linear range with a limit of determination of 8.7 μM was obtained for the detection of glucose. This work might provide a new approach to expose active sites for remarkable photoelectrochemical performance efficiently.

## Introduction

Enzyme-based biosensors are widely used in healthcare, especially in disease diagnosis and bioanalysis, mainly due to their high selectivity.[1,2] Photoelectrochemical (PEC) technologies are relative recently developed analytical methods, using a quite simple experimental setup, low background currents, and high sensitivity.[3–5] Photoelectrochemistry is electrochemically derived, thereby showing advantages such as even limit of determination (LOD) than those obtained for "traditional" electrochemical approaches.[6-8] PEC uses electrochemical processes to yield signals with high sensitivity and elevated accuracy with low background signal noise due to combination of light and electricity. [9–11] The combination of the photoelectrochemistry and enzymatic reaction processes allows the photoelectrochemical enzyme-based biosensors can combine the advantages from both approaches, mixing high selectivity and sensitivity.[12] Photoelectrochemical biosensors typically consist of bioactive material and a photoactive electrode substrate. The electrode substrate also functions as a signal transducer and a carrier for the biologically active material in the sensor.[13,14]

After the formation of the photoelectrochemical biosensor system, the change in the electrical signal can be mainly attributed to the mutual reaction of the photoelectrochemically active unit and the enzymatic product. Thus, the catalytic efficiency of the enzyme is equally essential. It is worth to be noted that the enzymatic efficiency mainly depends on the activity of the enzyme and the diffusion efficiency of products and substrates to the reaction center.[15] Nowadays, the immobilization of enzymes on the electrode has been significantly developed in terms of stability. Moreover, the combination of physical adsorption, cross-linking polymerization, and covalent bonds have made possible the in vitro applicability of enzymes.[16–19] However, in previously reported PEC enzyme-based biosensors, the utilization of enzymes is still low due to the lack of optimum spatial control of substrate and product diffusion.[20,21] Therefore, it is crucial to select an electrode material with excellent diffusion efficiency and a high turnover frequency (TOF).

Among many materials for photoelectric conversion, $TiO_2$ has received extensive attention due to its low toxicity, stability, and high catalytic activity. $TiO_2$ was already obtained in the form of nanotubes (NTs), nanorods, nanowires, and nanoribbons. The most popular form of $TiO_2$ at present is the nanotube-based structure, obtained mostly via anodization.[22] However, the nanotubes obtained through the anodized Ti foil not only have a low Ti foil utilization,[23] but also can have a lower in diffusion efficiency and TOF due to the low permeability of the sheet material. To obtain a structure that provides favorable properties for a sensor, this work used Ti wire mesh for anodization to obtain a 3D hollow-out $TiO_2$ nanowire cluster (NWc). Compared to the simple Ti foil, the network structure of

[a] State Key Laboratory of Marine Resource Utilization in South China Sea, College of Material Science and Engineering, Hainan University, Haikou 570228, China.
[b] School of Tropical Medicine and Laboratory Medicine, Key Laboratory of Emergency and Trauma of Ministry of Education, Hainan Medical University, Haikou 571199, China.
[c] State Key Laboratory of High-Efficiency Utilization of Coal and Green Chemical Engineering, School of Chemistry and Chemical Engineering, Ningxia University, Yinchuan 750021, China.
[d] Qiongtai Normal University, Haikou 571127, China.
†Electronic Supplementary Information (ESI) available: SEM, TEM, SEM-EDX spectra, XRD patterns, XPS spectra, Raman spectra and electrochemical measurement.
See DOI: 10.1039/x0xx00000x

Ti mesh can have a higher conducive to the exposure of active sites and the diffusion of substrates and products.

Taking into account the aspects mentioned above, we reported a 3D hollow-out $TiO_2$ NWc/GOx biosensor by using glucose oxidase (GOx) as a bioactive material. Amperometric i-t curve measurements showed that 3D hollow-out $TiO_2$ NWc/GOx biosensor could detect glucose with an ultrahigh sensitivity of 58.9 μA $mM^{-1}$ $cm^{-2}$. The unique hollow-out NWc structure increases the exposed area of the active sites, and the network structure considerably enhances the diffusion rate of the products and the substrate, thereby improving the efficiency of the enzymatic reaction. Meanwhile, the superior performance of the mesh electrode in the PEC glucose biosensor can provide an improved electrode structure for novel biosensor systems.

# Experimental

**Materials and reagents**

Ti wire mesh (50 mesh, 0.14 mm wire diameter, and 0.28 mm mesh width) was acquired from Kangwei Metal Wire Mesh Products Co., Ltd. (Hebei China). Ti sheets (thickness of 0.25 mm, 99.5% metal basis) were supplied by Alfa Aesar. GOx (EC 1.1.3.4, 5 KU·$mg^{-1}$ from Aspergillus niger) was purchased from Sangon Biotech. Other pharmaceutical reagents were of analytical grade.

**The synthesis of 3D hollow-out $TiO_2$ NWc.**

The Ti wire mesh was cut into small pieces (20 mm × 10 mm) and treated in a washing solution (HF: $HNO_3$: $H_2O$ = 1:4:5 in volume ratio) for 10 s. Then, the Ti wire mesh was ultrasonically treated in isopropanol, acetone, and ultrapure water respectively. Anodization (total area of etching, 10 mm × 10 mm) was carried out at room temperature for 90 min with a 20 V DC-regulated power supply. The working electrode was a Ti wire mesh, while the counter electrode was a Ti foil. The improved electrolyte formula consisted of 0.3 g $NH_4F$, 2 mL of water, and 88 mL of ethylene glycol. After the reaction, the sample was annealed at 400 °C in a muffle furnace for 3 h. Ti foil was also etched using the same anodization parameters, to form $TiO_2$ NTs as reference/for comparison.

**Immobilization of glucose oxidase on electrodes.**

The as-prepared 3D hollow-out $TiO_2$ NWc were placed on a piece of ultrasonically cleaned glass (20 mm × 10 mm). A total of 5 μL of chitosan (5 mg·$mL^{-1}$) and 5 μL of glucose oxidase (5 KU·$mL^{-1}$) were dropped on the anodized area and then dried at 4 °C in a fridge, overnight. After the solution solidified, the electrode was turned over, and dropwise add the same amount of solution (5 μL of chitosan and 5 μL of glucose oxidase) again. Lastly, the samples were dried at 4 °C in a fridge, overnight. For comparison, 10 μL of chitosan (5 mg·$mL^{-1}$) and glucose oxidase were added dropwise to the surface of the $TiO_2$ NTs electrode in a fridge, overnight.

**PEC measurements.**

Electrochemical investigations and biosignal conversions were performed using an electrochemical workstation (CHI Instruments, Chenhua CHI 852, Shanghai, China) with a 500 W xenon lamp (Beijing Zhongjiao Jinyuan Technology Co., Ltd., China). The test system was used with a three-electrode system (Pt sheet as a counter electrode and saturated Ag/AgCl reference electrode，bias of 0.4V，PBS electrolyte PH=7.4). During the measurement, the electrode was subjected to an optical density of 100 mW $cm^{-2}$.

**Instrumentation**

Scanning electron microscope (SEM) images were recorded with Hitachi SU 8010 (FESEM Hitachi, Japan), and and transmission electron microscope (TEM) images were acquired using JEOL JEM 2100. Characterization of the crystalline state of the samples was conducted via X-ray diffraction (XRD) (Model D/max 2550 V, Rigaku Co., Japan) using a diffractometer with monochromatized Cu Kα radiation (λ=1.5418 Å) over an angular range of 2θ=20°–90°. The sample was scanned at a speed of 0.01°/s at steps of 0.01°. The equipment was operated at 35 KV and 25 mA. The surface chemical composition of the prepared samples, such as 3D hollow-out $TiO_2$ NWc, was characterized by X-ray photoelectron spectroscopy (XPS) (Kratos: Axis Ultra DLD) with Al-Kα monochromated radiation as the excitation source. Raman spectra were collected using an Almega dispersive Raman system (Nicolet) and a Nd: YAG intracavity doubled laser operating at 532 nm with an incident power of 10 mW.

# Results and discussion

**Design guidelines of the 3D hollow-out $TiO_2$ NWc/GOx.**

The fabrication process of the 3D hollow-out $TiO_2$ NWc/GOx electrode is shown in Scheme 1A. Considering the relatively small diameter (~140 μm) of the cylindrical structure, the nanotube arrays of Ti wires, which were engraved with F- were broken by the strong interaction force of each other and were concentrated into clusters in the middle of Ti wires. Finally, a 3D hollow-out $TiO_2$ NWc structure was formed on the surface of the Ti wire mesh. After repeatedly immobilizing the enzyme two times, GOx reached a full coverage for each Ti wire. In order to more present more intuitively the structural advantages of 3D hollow-out $TiO_2$ NWc/GOx biosensors, the enzyme-based glucose PEC sensing strategy is revealed in Scheme 1B. The 3D network structure allows the enzyme to perform the enzymatic reaction on a higher surface (Scheme 1B (a, b, c)) on the electrode. On the other hand, the presence of meshes makes the diffusion of substrate and product around the enzyme more efficient.

**Microstructure of 3D hollow-out $TiO_2$ NWc electrode.**

The morphology and structure of 3D hollow-out $TiO_2$ NWc were elucidated in details by SEM analyses. Fig. 1A shows an enlarged view of the Ti wire mesh after calcination, where the structure of the titanium wire can be clearly observed. The uniform structure, pore diameter, and uniform thickness are particularly beneficial to the diffusion of the substance around the electrode. The SEM micrograph of a single anodized Ti wire is presented in Fig. 1B. The Ti wire had a diameter of approximately 140 μm, and a large number of sunkened

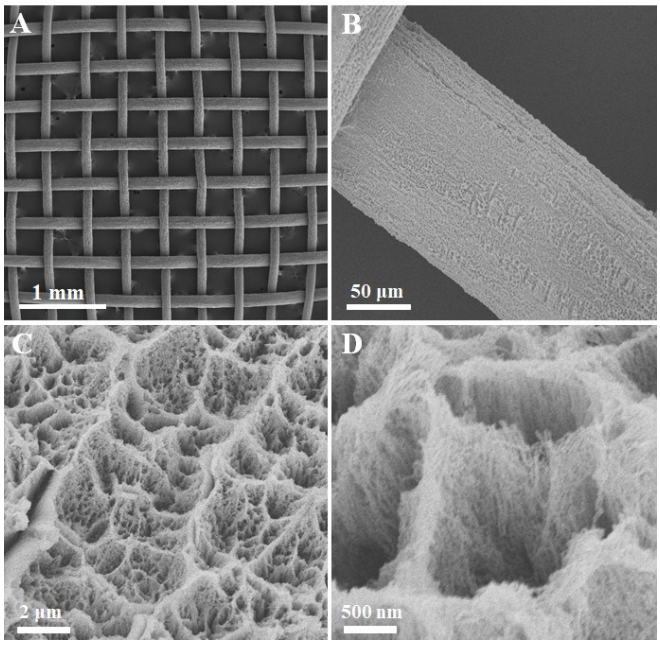


Fig. 1. SEM image of 3D hollow-out $TiO_2$ NWc electrode. (A) Magnified image of the Ti wire mesh with SEM. (B) Single Ti wire after anodization. (C, D) Images of 3D hollow-out $TiO_2$ NWc electrodes with different magnifications.

nanostructures were distributed on the surface. As shown in Fig. 1C, a large number of $TiO_2$ nanowires were assembled into many concave pore structures. The formation of the recessed nanowire stack structure can be attributed to the rough surface and large curving of the Ti wire. These properties caused a strong interaction of $TiO_2$ nanotubes during the etching process, which led to incomplete growth and fragmentation of the tubes. Many porous structures were formed due to the sparse packing of $TiO_2$ nanowires (Fig. 1D). The porous structure, especially the mesoporous structure, can enhance the enzyme loading efficiency and stability considerably and correspondingly, increasing its activity.[24-27] The image comparison before and after anodization is shown in Fig. S1 (ESI†).

**Characterization of 3D hollow-out $TiO_2$ NWc electrode.**

In order to ensure that the as-prepared materials are clean of contamination, EDS (Fig. 2A) and X-ray (Fig. 2B) diffraction measurements were performed on the $TiO_2$ nanomaterials synthesized in this work. The results from EDS measurements have shown that the prepared nano-materials are composed of $TiO_2$ compounds and do not contain other impurities. Moreover, as can be observed in Fig. 2B, all the peaks being observable on XRD patterns have matched precisely with the diffraction peak of $TiO_2$ in the anatase phase (JCPDS card number: 21–1272) and that of pure Ti (JCPDS card number: 44–1294).[28,29] These two results show that the as-synthesised nanomaterials in this work are pure $TiO_2$ of pure anatase phase. The high-resolution TEM image of a 3D hollow-out $TiO_2$ NWc is shown in Fig. S2A (ESI†). The lattice spacing of 0.35 nm in the figure corresponds to the anatase phase of $TiO_2$ (101), identified previously by the results of XRD. Fig. S2B (ESI†) shows the single crystal anatase structure of 3D hollow-out $TiO_2$ NWc through the SAED pattern.

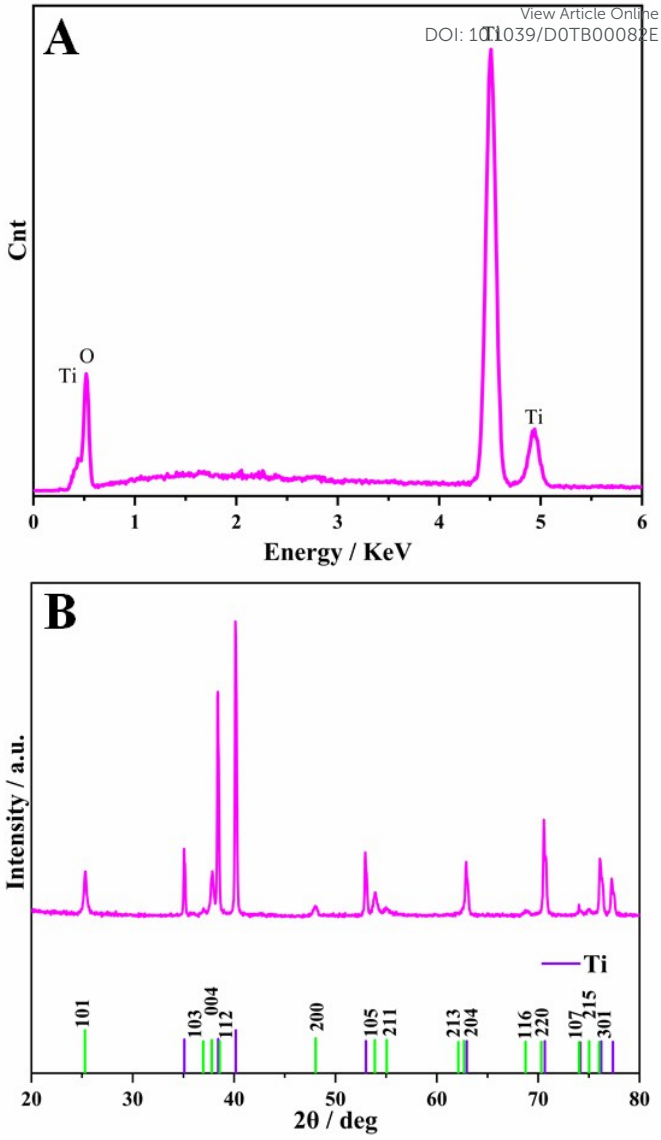


Fig. 2. (A) EDX spectra of 3D hollow-out $TiO_2$ NWc. (B) X-ray diffraction pattern (rose red) of $TiO_2$ nanomaterial synthesized in this study. The green line is the diffraction pattern of the standard anatase, and the purple line is the diffraction pattern of pure Ti.

Increasing the loading area of the enzyme is also one of the advantages of the 3D hollow-out $TiO_2$ NWc electrode. The SEM micrographs before and after loading the glucose oxidase are shown in Fig. S3 (ESI†). As can be observed in Fig. S3A (ESI†), $TiO_2$ NWc was coated with a film after loading the enzyme in comparison with the preloading stage (inset). On Fig. S3B (ESI†), the sunken structure on the Ti wire was evident, being attributed to the enzyme loading. Fig. S3 (C–F) (ESI†) shows that glucose oxidase was attached evenly on the surface of 3D hollow-out $TiO_2$ NWc structures. In order to more accurately show the loading of GOx on the $TiO_2$ NWc electrode, we performed EIS measurement of $TiO_2$ NWc before and after GOx loading. As shown in Fig. S4 (ESI†), the impedance of GOx-coated $TiO_2$ NWc electrodes is significantly higher, because the

presence of enzymes will reduce the conductivity of the electrodes.

In order to better analyze the composition state of the prepared electrode, the material composition and molecular state of 3D hollow-out $TiO_2$ NWc were analyzed by XPS and Raman spectroscopy, respectively. As shown in Fig. S5A (ESI†), the 3D hollow-out $TiO_2$ NWc electrode is composed of Ti and O, which is consistent with the EDS mapping image (Fig. 2A). The XPS spectrum of Ti 2p shows two main peaks, corresponding to Ti $2p_{1/2}$ at 464.6 eV and Ti $2p_{3/2}$ at 458.8 eV, which indicates that Ti exists as $Ti^{4+}$. The interval between the two peaks is 5.8 eV (Fig. S5B ESI†), which is consistent with previously reported XPS data.[30] As shown in Fig. S5C (ESI†), the O 1s spectrum can be fitted by two peaks. There is a higher binding energy peak near 531.7 eV, which is attributed to -OH, while another lower binding energy peak is about 530.1 eV, which is attributed to O (Ti-O-Ti) in the crystal lattice.[31] Raman spectroscopy is further used to characterize the electrodes constructed (Fig. S5D ESI†). The materials in the electrodes exhibit typical Raman vibration modes of anatase $TiO_2$, namely, 141 (Eg), 395 (B1g), 516 (A1g), and 638 $cm^{-1}$ (Eg). It is worth noting that the black line is the standard Raman spectrum of commercial anatase $TiO_2$. Comparing the two curves, it is easy to see that the Eg peak at 141 $cm^{-1}$ shifted, which may be due to the residual fluorine during the anodization.

**Electrochemical measurement of 3D hollow-out $TiO_2$ NWc electrode.**

In order to evaluate the catalytic performance of the 3D hollow-out nanowire cluster structures, we have performed a turnover frequency (TOF) calculation on the electrodes.

$$2h^{+}+H_2O_2=O_2+2H^{+}$$

The TOF value represents the number of molecules converted at each active site per unit time, and the higher TOF value means increased catalytic efficiency. The TOF value is estimated based on the following two equations:[32-34]

$$n=Q/(2F)$$

$$TOF=I/(2Fn)$$

Where Q is the voltammetric charge (shown in Fig. S6 ESI†), F is the Faraday constant (96485 C $mol^{-1}$), I is the current (A) measured during the linear sweep measurement, and n is the number of active sites (mol). The factor of 1/2 in the equation means that two holes ($h^{+}$) are needed to reduce the hydrogen peroxide to one oxygen.

The large electroactive area can significantly improve the catalytic performance of the electrode.[35] As shown in Fig. S7A (ESI†), measurements involving cyclic voltammetry were performed from 20 – 200 $mV \cdot s^{-1}$ at different rates in 10 mM $Fe(CN)_6^{3-/4-}$ solution (0.1 M KCl). The effective area of the 3D hollow-out $TiO_2$ NWc electrode was calculated using the Randles–Sevcik equation,[36,37] as follows:

$$Ip = (2.69\times10^5)\, n^{3/2}\, AD^{1/2}\, v^{1/2}C_0,$$

where Ip is the peak current, n is the number of electrons transferred in the redox process (here, n = 1), $C_0$ is the $Fe(CN)_6^{3-/4-}$ concentration in the electrode, A represents the effective surface area, D is the diffusion coefficient ($7.6\times10^{-6}$ $cm^2\ s^{-1}$), and v is the scan rate. After calculation, as shown in Fig. S7B (ESI†), the calculated value of A is 2.71 $cm^2$. Compared with the surface area of 1.619 $cm^2$ of the Ti wire mesh, the electroactive area of the 3D hollow-out $TiO_2$ NWc electrode reaches 2.71 $cm^2$, proving the advantage of the nanowire cluster structure in exposing active sites.

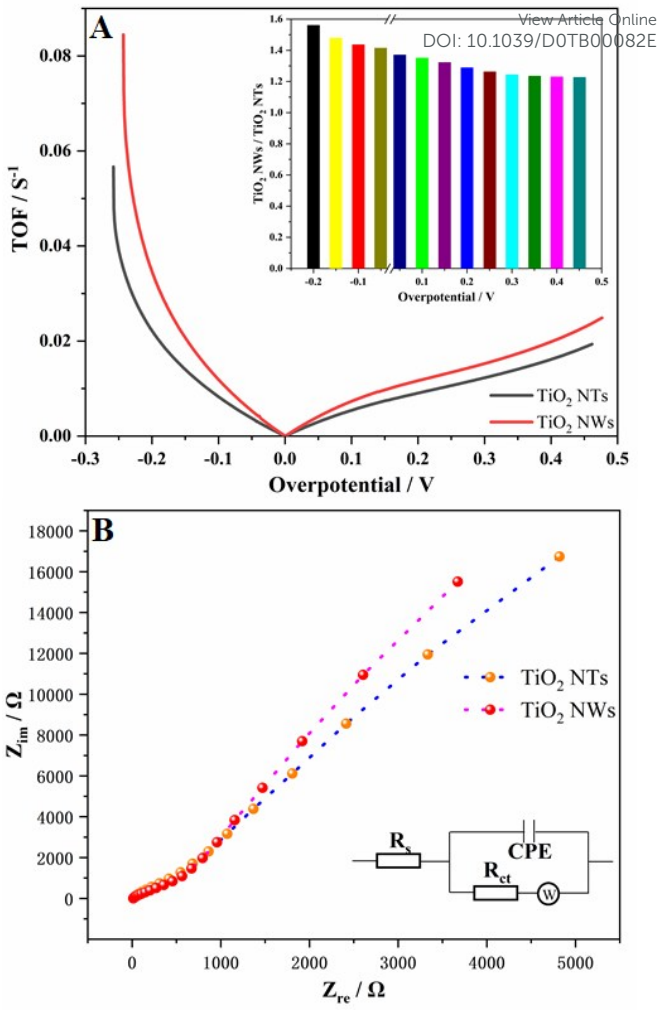


Fig. 3. (A) Comparison of the TOFs of $TiO_2$ NWc and $TiO_2$ NTs. The inset graph shows the TOF values of $TiO_2$ NWc / $TiO_2$ NTs. (B) Nyquist plots of $TiO_2$ NWc and $TiO_2$ NTs in 0.1 M PBS (PH=7.4). The inset image illustrates the equivalent circle model of the system.

The TOF vs. overpotential curves for $TiO_2$ NWc and $TiO_2$ NTs are shown in Fig. 3A. It can be seen, the $TiO_2$ NWs curve is the highest, indicating that $TiO_2$ NWs can convert more hydrogen peroxide at the same time, compared to $TiO_2$ NTs. Besides, it can be seen from the inset of Fig. 3A that $TiO_2$ NWs have higher TOF in the negative pressure range, indicating that 3D hollow-out $TiO_2$ NWc has a stronger catalytic activity. This also lays a possible theoretical foundation for the multifunctional application (HER, e.g.) of 3D hollow-out nanowire cluster structures. The Electrochemical Impedance Spectroscopy was used to analyze the diffusion resistance of the electrode. As for the low-frequency region, the Warburg impedance (W) of the curves were calculated to be 824.1 $\Omega \cdot S^{1/2}$ and 1086 $\Omega \cdot S^{1/2}$ for $TiO_2$ NWc and $TiO_2$ NTs, respectively (Fig. 3B). The hollow-out nanowire cluster structured materials exhibit much lower W values than the unmodified materials, indicating improved mass diffusion kinetics of the electrodes. This may be due to the network structure of the hollow-out nanowire clusters, being more efficiently passed by the electrolyte and reacting faster near the electrodes. The TOF calculations and diffusion kinetics

View Article Online
DOI: 10.1039/D0TB00082E



verification have also demonstrated the excellent catalytic ability and enhanced diffusion ability of 3D hollow-out $TiO_2$ NWc.

The unique mesh structure of Ti mesh provided excellent control for product and substrate diffusion, but this structure also had a large light leakage area (~0.67 $cm^2$), as the photoactive area of the Ti wire was only ~0.33 $cm^2$. Amperometric i-t curve tests were performed on 3D hollow-out $TiO_2$ NWc and $TiO_2$ NTs, and the results are shown in Fig. S8A (ESI†).

The photocurrent intensity of $TiO_2$ NTs alone was ~2.4-fold higher than those for 3D hollow-out $TiO_2$ NWc. For $TiO_2$ NTs with a 3-fold increase in the photoactive area, an approximately 2.4-fold increase in photocurrent was insufficient. The 3D hollow-out $TiO_2$ NWc unit area photocurrent intensity was dominant, which can also prove by Fig. S8B (ESI†). The 3D hollow-out $TiO_2$ NWc electrode performed better under the same conditions, possibly because hollow-out and nanowire cluster structures exposing more active sites in comparison with closed sheet structure.

The effect of the presence or absence of glucose and irradiation with the light on the photoelectric response of 3D hollow-out $TiO_2$ NWc/GOx biosensors were also evaluated via cyclic voltammetry (CV) and linear sweep voltammetry (LSV). The 3D hollow-out $TiO_2$ NWc/GOx biosensors exhibited a small background current response at 0.4 V bias with neither glucose nor illumination (Fig. S9A (a) ESI†). When exposed to light (Fig. S9A (c) ESI†), the photocurrent rose with the increase of the applied voltage, which indicated that the 3D hollow-out $TiO_2$ NWc/GOx biosensors had strong light absorption and electron-hole separation ability. As shown in Fig. S9A (b) (ESI†), the obtained photocurrent of 3D hollow-out $TiO_2$ NWc/GOx biosensors hardly changed in the absence of light, even with the addition of 2 mM glucose. These results showed that glucose could only increase the photocurrent of 3D hollow-out $TiO_2$ NWc/GOx biosensors under illumination. This was also confirmed, as the maximum photocurrents of 3D hollow-out $TiO_2$ NWc/GOx biosensors were reached in the presence of both glucose and light, as shown in Fig. S9A (d) (ESI†), indicating that 3D hollow-out $TiO_2$ NWc/GOx biosensors had low background signal and interference. The CV measurement results also illustrate the above results (Fig. S9B ESI†).

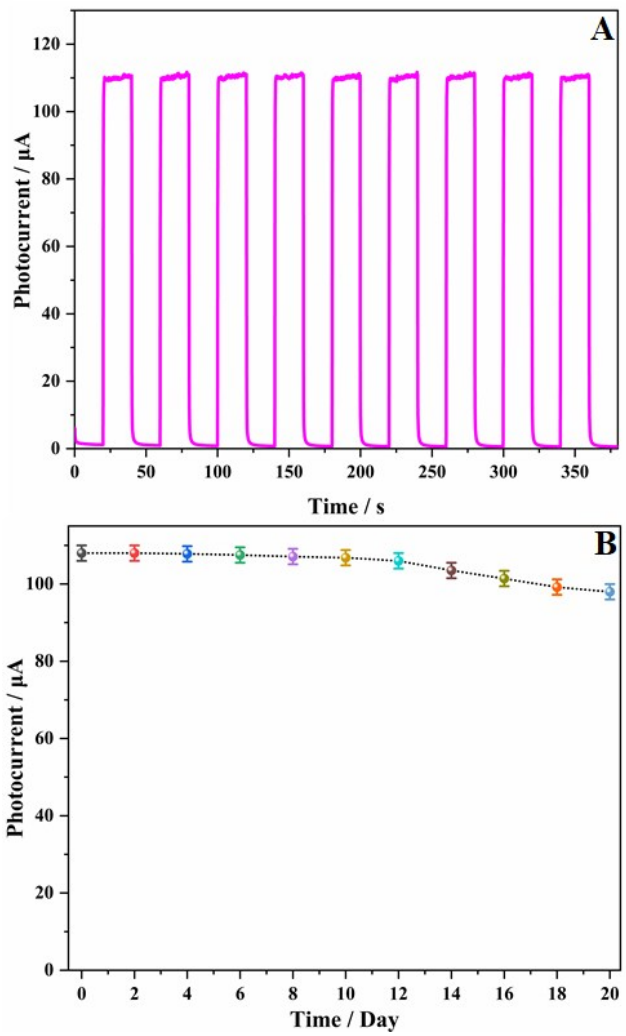


Fig. 5. (A) Stability under lights on conditions (presence of 1 mM glucose). (B) Long-term (20 days) stability test of 3D hollow-out $TiO_2$ NWc/GOx biosensor in 0.1 M PBS electrolyte (pH of 7.4).

Fig. 4. (A) Time–current density responses of 3D hollow-out $TiO_2$ NWc/GOx toward Glu at an increasing concentration from 0 mM to 2 mM in the electrolyte of 0.1 M PBS (pH of 7.4). (B) Linear calibration ([Glu] vs. photocurrent density) curve.

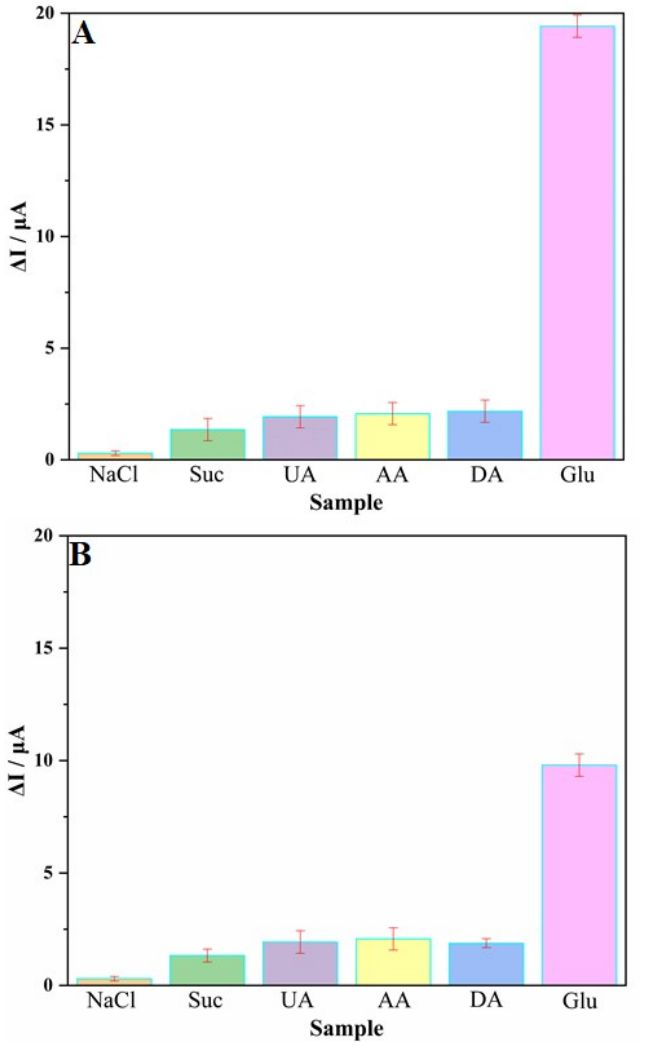


**Sensing measurement of 3D hollow-out $TiO_2$ NWc/GOx biosensor.**

The photoelectrochemical biosensor performance was calculated based on the photocurrent density-time curve. It can be seen from Fig. 4A that after exposure to light, the photocurrent of the electrode rapidly increases, and the response time is <1 second. After adding glucose solutions with different concentration, the photocurrent of the electrode increased steadily without much fluctuation, which indicates that the sensor also has better stability during a single measurement. The photoelectrochemical amperometric i-t curve test of the 3D hollow-out $TiO_2$ NWc/GOx biosensor was conducted at different concentrations of glucose. In the presence of different glucose concentrations, the photo-

Fig. 6. Compare the anti-interference performance of (A) 3D hollow-out $TiO_2$ NWc/GOx and (B) $TiO_2$ NWc/GOx biosensors. The experiment was conducted in 0.1 M PBS (pH of 7.4) with 0.1 mM of NaCl, sucrose (Suc), uric acid (UA), ascorbic acid (AA), and dopamine (DA) and 1 mM glucose.

generated holes on the 3D hollow-out $TiO_2$ NWc/GOx biosensor can react with the $H_2O_2$ produced by the enzymatic reaction of

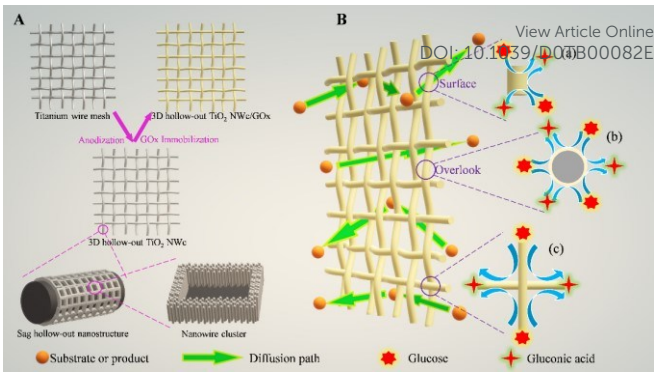


glucose oxidase, resulting in different levels of an electrical signal (mechanism in Fig. S10 ESI†). As shown in Fig. 4B, the linear equation represents the regression equation for photocurrent (μA) = 58.9 [Glu] (mM) + 264.5 ($R^2$ = 0.99903). The 3D hollow-out $TiO_2$ NWc/GOx biosensor had a linear range of 0–2 mM, a sensitivity of 58.9 μA $mM^{-1}$ $cm^{-2}$, and a limit of determination (LOD) of 8.7 μM (S/N = 3).

The same glucose PEC measurement was performed on $TiO_2$ NTs, as reference. The result of the measurement is shown in Fig. S11 (ESI†). Compared with the 3D hollow-out $TiO_2$ NWc/GOx biosensor, the sensitivity of the $TiO_2$ NTs/GOx biosensor was extremely low possibly due to the relatively sealed structure of the flaky $TiO_2$ NTs, which caused the active sites to be hidden and the diffusion efficiency to be low.[38-41]

The stability of the 3D hollow-out $TiO_2$ NWc/GOx biosensor on the 400 s of short time-current curve measurement with 1 mM glucose is shown in Fig. 5A. When the light was turned on, the photocurrent rapidly increased and stabilized. After nine cycles, the photocurrent of the 3D hollow-out $TiO_2$ NWc/GOx biosensor also had 99.73% of the initial value, which was remarkably stable in a short time. To monitor the long-term stability of the biosensor, we have performed 1 mM glucose measurement every 2 days (store at 4 ℃ for the rest of the time). As shown in Fig. 5B, after a long cycle of 20 days, the photocurrent of the 3D hollow-out $TiO_2$ NWc/GOx biosensor had an initial value of 91.48%. These results showed that the 3D hollow-out $TiO_2$ NWc/GOx biosensor had good stability.

Fig. 6A shows the interference measurements of 3D hollow-out $TiO_2$ NWc/GOx biosensor on glucose-compatible substances (NaCl, sucrose, uric acid, ascorbic acid, and dopamine). When the glucose and interferents are in correlation with the concentrations observable of human blood, the 3D hollow-out $TiO_2$ NWc/GOx biosensor has ~8 times better photoelectric response to glucose than other interferents. However, the $TiO_2$ NTs/GOx biosensors under the same parameters had smaller performance, in this case, only achieving ~4 times the photoelectric response to glucose (Fig. 6B). This result indicates that the $TiO_2$ NWc structure has better selectivity than the $TiO_2$ NTs structure for glucose.

View Article Online
DOI: 10.1039/D0TB00085E



Table 1 shows the performance of the 3D hollow-out $TiO_2$ NWc/GOx biosensor compared with that of other glucose sensors. Compared to previously reported structures, the advantages of 3D hollow-out nanowire cluster structures in improving sensitivity are huge.

**Table. 1**. Performance comparison among different glucose sensors.

| Electrode construction | LOD | Linear range | Sensitivity | Ref. |
|---|---|---|---|---|
| **3D $TiO_2$@$Cu_2O$@Ni** | 1 µM | 0.002–10 mM | – | [42] |
| **ITO/$TiO_2$-$Co_3O_4$-CNT-GOx** | 0.16 µM | 0–4 mM | 0.3 µA $mM^{-1}cm^{-2}$ | [43] |
| **ITO/$TiO_2$–$MoS_2$–GOx** | 15 µM | 0.1–10 mM | 0.81 µA $mM^{-1}cm^{-2}$ | [44] |
| **FTO/ $Fe_2O_3$–NB–PDA–GDH** | 25.2 µM | 0–2 mM | 7.36 µA $mM^{-1}\,cm^{-2}$ | [45] |
| **Glass/$BaTiO_3$ (enzyme-less)** | 7.941 µM | 0.0001–1 mM | 23.79 µA $mM^{-1}\,cm^{-2}$ | [46] |
| **3D hollow-out $TiO_2$ NWc/GOx** | 8.7 µM | 0–2 mM | 58.9 µA $mM^{-1}\,cm^{-2}$ | This work |

*All the analyte used in the table is glucose.

Scheme 1. (A) Preparation process of 3D hollow-out $TiO_2$ NWc/GOx electrode. (B) PEC sensing mechanism of 3D hollow-out $TiO_2$ NWc/GOx for glucose. Among them, insets (a), (b), and (c) are intended to show that the space utilization of the enzymatic reaction can be extremely high.

## Conclusions

A novel construction of 3D hollow-out $TiO_2$ NWc glucose biosensor was proposed that can achieved an ultra-high sensitivity of 58.9 µA $mM^{-1}$ $cm^{-2}$ in a photoelectrochemical enzymatic sensor system. Considering the reticular structure and large active site exposure area of the 3D hollow-out $TiO_2$ NWc electrode, the enzymatic reaction can be carried out with increased efficiency. The improvement of enzyme stability by the hollow-out structure promoted the permanence of the sensing system. Complete encapsulation of the electrode against the enzyme also contributed remarkably to the selectivity of the sensing system. Based on proof of concept, we have established a new sensing strategy using immobilized enzymes to achieve breakthrough performance in photoelectrochemical enzymatic sensors. Moreover, this study also provides the potential for the industrial applications of photoelectrochemical enzyme-based sensors.

## Conflicts of interest

There are no conflicts to declare.

## Acknowledgements

This research was financially supported by the Finance Science and Technology Project of Hainan Province (ZDYF2018106, 2019RC221), National Natural Science Foundation of China (51762012, 81860373), Key Laboratory Open Project Fund of Hainan University (2018008), and Research Unit of Island Emergency Medicine of Chinese Academy of Medical Sciences (2019RU013).

## References

1 W.-W. Zhao, J.-J. Xu, H.-Y. Chen, *Chem. Soc. Rev.*, 2015, **44**, 729-741.
2 O. S. Kwon, H. S. Song, T. H. Park, J. Jang, *Chem. Rev.*, 2019, **119**, 36-93.
3 L. Zhao, J. Ji, Y. Shen, K. Wu, T. Zhao, H. Yang, Y. Lv, S. Liu and Y. Zhang, *Chem. Eur. J.*, 2019, **25**, 15680-15686.
4 R. Gill, M. Zayats, I. Willner, Angew. Chem. Int. Ed., 2008, **47**, 7602-7625.
5 Q. Zhou, G. Li, K. Chen, H. Yang, M. Yang, Y. Zhang, Y. Wan, Y. Shen and Y. Zhang, *Anal. Chem.*, 2020, **92**, 983-990.
6 K. J. Babu, T. R. kumar, D. J. Yoo, S.-M. Phang and G. G. kumar, *ACS Sustainable Chem. Eng.*, 2018, **6**, 16982-16989.
7 K. Vasuki, G. Siva, A. Balasubramani, M. Pannipara, A. G. Al-Sehemi, Y. Xia, R. Fang, D. J. Yoo, T. R. Kumar, R. Ramachandran and G. G. kumar, *Appl. Phys. A.*, 2019, **125**, 384.
8 P. Vennila, D. J. Yoo, A. R. Kim and G. G. kumar, *J. Alloys Compd.*, 2017, **703**, 633-642.
9 J. Tang, B. Kong, Y. Wang, M. Xu, Y. Wang, H. Wu, G. Zheng, *Nano Lett.*, 2013, **13**, 5350-5354.
10 E. Golub, G. Pelossof, R. Freeman, H. Zhang, I. Willner, *Anal. Chem.*, 2009, **81**, 9291-9298.
11 Q. Zhou, H. Xue, Y. Zhang, Y. Lv, H. Li, S. Liu, Y. Shen and Y. Zhang, *ACS Sensors.*, 2018, **3**, 1385-1391.
12 W.-W. Zhao, J.-J. Xu, H.-Y. Chen, *Biosens. Bioelectron.*, 2017, **92**, 294-304.
13 N. Muthuchamy, K. P. Lee, A. I. Gopalan, *Biosens. Bioelectron.*, 2017, **89**, 390-399.
14 A. I. Gopalan, N. Muthuchamy, K. P. Lee, *Biosens. Bioelectron.*, 2017, **89**, 352-360.

15 P. Li, Q. Chen, T. C. Wang, N. A. Vermeulen, B. L. Mehdi, A. Dohnalkoya, N. D. Browning, D. Shen, R. Anderson, D. A. Gomez-Gualdron, F. M. Cetin, J. Jagiello, A. M. Asiri, J. F. Stoddart, O. K. Farhal, *Chem.*, 2018, **4**, 1022-1034.

16 H. E. Schoemaker, D. Mink, M. G. Wubbolts, *Science (New York, N.Y.)*., 2003, **299**, 1694-1697.

17 Y. H. P. Zhang, S. Myung, C. You, Z. Zhu, J. A. Rollin, *J. Mater. Chem.*, 2011, **21**, 18877-18886.

18 R. A. Sheldon, S. van Pelt Chem. Soc. Rev. 2013, **42**, 6223-6235.

19 A. Kuchler, M. Yoshimoto, S. Luginbuhl, F. Mavelli, P. Walde, *Nature Nanotech.*, 2016, **11**, 409-420.

20 C. Garcia-Galan, A. Berenguer-Murcia, R. Fernandez-Lafuente, R. C. Rodrigues, *Adv. Synth. Catal.*, 2011, **353**, 2885-2904.

21 S. F. M. van Dongen, M. Nallani, J. L. L. M. Cornelissen, R. J. M. Nolte, J. C. M. van Hest, *Chem. Eur. J.*, 2009, **15**, 1107-1114.

22 J. Bai, B. Zhou, Chem. Rev., 2014, **114**, 10131-10176.

23 C. Grimes and G. Mor, *Optical & Electronic Materials; Springer: New York.*, 2009, p5.

24 D. Van Gough, A. Wolosiuk, P. V. Braun, *Nano Lett.*, 2009, **9**, 1994-1998.

25 R. Qian, L. Ding, H. Ju, *J. Am. Chem. Soc.*, 2013, **135**, 13282-13285.

26 I. Ortac, D. Simberg, Y.-s. Yeh, J. Yang, B. Messmer, W. C. Trogler, R. Y. Tsien, S. Esener, *Nano Lett.*, 2014, **14**, 3023-3032.

27 H. S. Kim, S.-G. Hong, K. M. Woo, V. T. Seijas, S. Kim, J. Lee, J. Kim, *Acs Catalysis.*, 2018, **8**, 6526-6536.

28 H. G. Yang, C. H. Sun, S. Z. Qiao, J. Zou, G. Liu, S. C. Smith, H. M. Cheng, G. Q. Lu, *Nature.*, 2008, **453**, 638-641.

29 H. G. Yang, H. C. Zeng, *J. Phys. Chem. B*, 2004, **108**, 3492-3495.

30 B. Banerjee, V. Amoli, A. Maurya, A. K. Sinha and A. Bhaumik, Nanoscale, 2015, **7**, 10504-10512.

31 J. Sun, W. Wen and J. M. Wu, J. Am. Ceram. Soc., 2013, **96**, 2109-2116.

32 J. Wang, F. Xu, H. Jin, Y. Chen, Y. Wang, *Adv. Mater.*, 2017, **29**. 1605838.

33 J. Kibsgaard, T. F. Jaramillo, *Angew. Chem. Int. Ed.*, 2014, **53**, 14433-14437.

View Article Online
DOI: 10.1039/D0TB00082E

34 E. J. Popczun, J. R. McKone, C. G. Read, A. J. Biacchi, A. M. Wiltrout, N. S. Lewis, R. E. Schaak, *J. Am. Chem. Soc.*, 2013, **135**, 9267-9270.

35 R. Atchudan, N. Muthuchamy, T. N. J. I. Edison, S. Perumal, R. Vinodh, K. H. Park, Y. R. Lee, *Biosens. Bioelectron.*, 2019, **126**, 160-169.

36 R. Zhang, J. Bao, Y. Pan, C.-F. Sun, *Chem. Sci.*, 2019, **10**, 2604-2612.

37 D. Y. W. Yu, C. Fietzekb, W. Weydanzb, K. Donouea, T. Inouea, H. Kurokawaa, S. Fujitania, *J. Electrochem. Soc.*, 2007, **154**, A253-A257.

38 K. Liang, R. Ricco, C. M. Doherty, M. J. Styles, S. Bell, N. Kirby, S. Mudie, D. Haylock, A. J. Hill, C. J. Doonan, P. Falcaro, *Nat. Commun.*, 2015, **6**. 7240.

39 F.-K. Shieh, S.-C. Wang, C.-I. Yen, C.-C. Wu, S. Dutta, L.-Y. Chou, J. V. Morabito, P. Hu, M.-H. Hsu, K. C. W. Wu, C.-K. Tsung, *J. Am. Chem. Soc.*, 2015, **137**, 4276-4279.

40 F. Lyu, Y. Zhang, R. N. Zare, J. Ge, Z. Liu, *Nano Lett.*, 2014, **14**, 5761-5765.

41 H. Deng, S. Grunder, K. E. Cordova, C. Valente, H. Furukawa, M. Hmadeh, F. Gandara, A. C. Whalley, Z. Liu, S. Asahina, H. Kazumori, M. O'Keeffe, O. Terasaki, J. F. Stoddart, O. M. Yaghi, *Science*, 2012, **336**, 1018-1023.

42 Y.-C. Zhu, Y.-L. Liu, Y.-T. Xu, Y.-F. Ruan, G.-C. Fan, W.-W. Zhao, J.-J. Xu, H.-Y. Chen, *Acs. Appl. Mater. Inter.*, 2019, **11**, 25702-25707.

43 B. Cakiroglu, M. Ozacar, *Biosens. Bioelectron.*, 2018, **119**, 34-41.

44 X. Liu, X. Huo, P. Liu, Y. Tang, J. Xu, X. Liu, Y. Zhou, *Electrochim. Acta.*, 2017, **242**, 327-336.

45 G. M. Ryu, M. Lee, D. S. Choi, C. B. Park, *J. Mater. Chem. B.*, 2015, **3**, 4483-4486.

46 S. Selvarajan, N. R. Alluri, A. Chandrasekhar, S.-J. Kim, *Sensor. Actuat. B-Chem.*, 2016, **234**, 395-40

View Article Online
DOI: 10.1039/D0TB00082E

# Table of Contents Entry

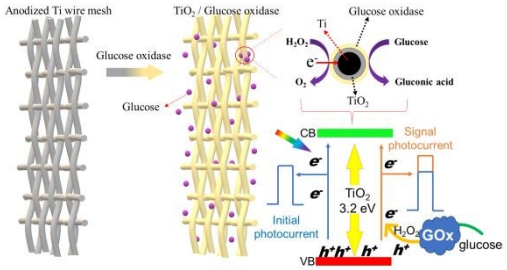


The reticulate $TiO_2$ nanowire cluster electrode demonstrated higher sensitivity performance due to enhanced diffusion effect and more active sites.